Experimental investigation of the nonlinear response of turbulent premixed flames to imposed inlet velocity oscillations

R. Balachandran [a], B.O. Ayoola [b], C.F. Kaminski [b], A.P. Dowling [a], E. Mastorakos [a,*]

[a] *Department of Engineering, University of Cambridge, UK*
[b] *Department of Chemical Engineering, University of Cambridge, UK*

Abstract

This paper describes an experimental investigation of acoustically forced lean premixed turbulent bluff-body-stabilised flames in an enclosure short enough so that no coupling of the combustor downstream acoustics occurred for the frequencies studied here, which allows an unambiguous examination of the flame response to inlet velocity fluctuations. Special emphasis was placed on the amplitude dependence of this response. Measurements of the heat release rate were performed with OH^* and CH^* chemiluminescence, planar laser-induced fluorescence (PLIF) of OH from which the flame surface density (FSD) was computed, and simultaneous CH_2O and OH PLIF imaging from which the local heat release rate (RX) was estimated. The global heat release measured with chemiluminescence and that integrated from the local FSD measurements were in close agreement, while a comparison between FSD and high-resolution RX imaging also showed good agreement. This suggests that estimates of the flame area are sufficient to determine heat release rate for this flow. The heat release response became nonlinear after inlet velocity amplitudes of around 15% of the bulk velocity. This value depended on the forcing frequency and the equivalence ratio. The nonlinearity was found to occur when the shear layers rolled up into vortices. The vortices induced by the inlet velocity fluctuations not only generated flame area when the flame wrapped around them, but also caused cusps and even large-scale flame annihilation events, as observed in time-resolved OH PLIF images. Such events occurred when parts of the flame stabilised on the inner shear layer close to the recirculation zone collapsed on parts of the flame stabilised on the outer recirculation zone, a phenomenon that was made more prominent with increasing forcing amplitude. A further nonlinearity occurred at high amplitudes and at some equivalence ratios, where a significant leakage of energy to higher harmonics was observed, but the origin of this is not yet clarified. The present results suggest that the flame sheet kinematics play a major role in the saturation mechanism of lean premixed flame response, hence extending previous experimental and analytical results from laminar to turbulent flames. Heat release fluctuations due to local fluctuations of strain rate and curvature were less significant, while no localised extinction has been observed even at large forcing amplitudes.
© 2005 The Combustion Institute. Published by Elsevier Inc. All rights reserved.

---

* Corresponding author.
 E-mail address: em257@eng.cam.ac.uk (E. Mastorakos).

1. Introduction

The theoretical description of combustion-induced oscillations, a problem of significant theoretical and practical importance, necessitates a quantification of the response of the flame to the unsteady inlet velocity and/or equivalence ratio caused by the pressure waves that may be set up in the combustor. This is usually done by the flame transfer function (H) [1–16]. If the instantaneous flow velocity at the burner exit is U, then $U(t) = \langle U \rangle + u'(t)$, where $\langle \ \rangle$ and primes represent the mean and the fluctuating components, respectively. Similarly, if Q is the heat release rate, $Q(t) = \langle Q \rangle + Q'(t)$. For completely premixed mixtures, the nonlinear flame transfer function or nonlinear frequency response function can then be defined as $H(f, A)$,

$$H(f, A) = \frac{Q'(f)/\langle Q \rangle}{u'(f)/\langle U \rangle}, \tag{1}$$

where $\langle Q \rangle$ is the time-averaged heat release rate, $\langle U \rangle$ is the bulk velocity of the mixture entering the combustor, $Q'(f)$ and $u'(f)$ are their corresponding amplitudes at frequency f (i.e., the amplitudes of the Fourier transforms of Q and U, narrow-band filtered around f) and A is the magnitude of $u'(f)/\langle U \rangle$. If H were available, then reduced-order models (for a recent review of this concept, see [1]) could be advantageously deployed to predict the onset of instabilities. H has been determined by theoretical models [1–8] and CFD [9,10], but very few direct measurements of H are available [11–16] due to the difficulties involved in estimating the heat release rate. Although the earlier linear models [1,7] for predicting combustion instabilities could predict the phase relationships well even with rough estimates of H, more accuracy is required on the amplitude dependence of H for limit-cycle amplitude predictions.

Until now, most heat release measurements have been based on narrow-band OH^*, CH^*, C_2^* and broadband C_2^* chemiluminescence emission [11–19]. Langhorne [11] used light emission from C_2^* to quantify the heat release and investigated "Reheat Buzz" in a premixed flame stabilised by V-gutter. The measurements were used to obtain heat release–pressure transfer function, which was later used for theoretical predictions successfully [12]. OH^* chemiluminescence was used to measure the transfer function to understand the combustion dynamics of turbulent swirling flames [14] and was also used later successfully by Zähringer et al. [15] to measure the transfer function

in a practical industrial burner. Further, Lieuwen and Neumeier [16] measured nonlinear transfer function in a gas turbine combustor using OH^* chemiluminescence. Lawn [17] developed a cross-correlation technique based on OH^* chemiluminescence to measure the distributed heat release in unsteady flames. Pun et al. [18] used OH^* as well as OH PLIF to measure the flame response and Bernier et al. [19] used CH^* to quantify the heat release for their study in a model premixed, prevaporised swirl-stabilised combustor. In all the above studies, the chemiluminescence signals have been observed to scale linearly with fuel consumption rates and have thus been assumed to correlate with global heat release rates. CH^* was used to understand also the response of forced nonpremixed flames by Hardalupas and Selbach [20]. In a recent study with opposed jet flames [21], the authors conclude that OH^*, CH^*, and CO_2^* are better heat release measures as opposed to the C_2^* chemiluminescence, which was reported to fail under high strain conditions.

In earlier experimental studies with CH PLIF it was found that CH disappears in regions of high curvature and rates of strain [22]. By inference, both CH^* and OH^* must be questioned for their reliability as heat release or flame front markers, because both are products of the CH reaction pathway. Similar problems exist for CO_2^* chemiluminescence. A thorough recent review of related theoretical and experimental work by Lee and Santavicca [23] with relevance to instability research also suggests that chemiluminescence data must be interpreted with care. However, very few investigations were dedicated to compare the dynamic response of the flame chemiluminescence with other advanced optical measurements.

In parallel to theoretical models that use a calculation of flame surface area to build the flame transfer function (see [24] and the reviews [2,7]), measurements of the flame area have been performed for laminar flames [4–6] but not extensively yet for turbulent flames. Various techniques can be used to visualise the flame contour and hence flame area. For premixed flames, OH PLIF is very powerful since OH gradients are generally found to correlate well with the position of the local flame front [23,25–27]. Knikker et al. [25] performed OH PLIF in a bluff-body-stabilised, ducted premixed turbulent flame to identify the two-dimensional flame contours and hence to estimate heat release rates from them. To get an estimate of heat release from the flame area, one must assume that the flame speed does not change along the flame

contour. In addition, the total flame area is difficult to estimate from two-dimensional image slices because no information on the effects of wrinkling in the third dimension is available. Hence, there are ambiguities in estimates of the total heat release from such data. Despite these reservations, Ref. [23] reported measurements of two-dimensional flame contours, which were identified from OH PLIF images in an unstable flame in a gas turbine combustor and the resulting estimated total flame area was found to be in phase with CO_2^* emission. Since FSD has already been proven a very useful tool for turbulent combustion in general [28,29] and can be captured equally well by tomography [28–30] and OH PLIF [31,32], this technique can be used for flame instability studies, provided that the burning rate along the flame contour does not change significantly.

A more direct measurement of local heat release rate can be accomplished by simultaneous PLIF imaging of formaldehyde (CH_2O) and OH. The pixel-by-pixel product of such images has been shown to correlate well with the local heat release rate in studies of laminar flame–vortex interactions [33,34]. Böckle et al. [35] have demonstrated the technique in turbulent premixed flames stabilised on a Bunsen burner and Fayoux et al. [36] used it in laminar counterflow premixed flames. It was suggested in Ref. [37] that this technique predicts the heat release better than chemiluminescence in the presence of strong vortex, which makes this technique a better candidate for conditions where the flame–acoustics interaction is dominated by vortex shedding mechanisms.

In the present paper, we apply the above methods of heat release measurement to derive flame transfer functions for acoustically forced premixed turbulent flames. The difficulties discussed above are expected to be more pronounced when large-amplitude oscillations are present, with resulting high strain rates and possible localised extinctions. Very few experimental investigations of this so-called "nonlinear" regime are available (e.g., [16,38]), although it is a condition that may occur in combustion-induced oscillations in realistic combustors and is related to the combustor's limit-cycle behaviour. The saturation of the flame response to flow velocity fluctuations is challenging to describe theoretically [3] and little is known about its physical origin, although its presence has been observed in naturally unstable combustors [39–41]. There have been numerous investigations on small-amplitude perturbations both by experimental determination and by modelling (see [4–7]), however the information about finite amplitude effects on frequency response of flame is very scarce. Dowling [3] modelled the nonlinear coupling between inlet velocity fluctuations and heat release based on the fact that the chemiluminescence cannot become negative dur-

ing the flow reversals, leading to conditions where the saturation happens when the flow velocity fluctuations are of the order of mean velocity, i.e., $A \sim 1$. The measurements in a lean turbulent premixed flame by Bellows et al. [38] showed a saturation in their flame chemiluminescence at a velocity amplitude of $A \sim 0.2$–0.3. They speculated that the nonlinear response could be due to nonlinear flame sheet kinematics, but suggested further optical studies of the flame front dynamics to better understand the mechanism present in their study. Theoretical and experimental determination of transfer function in laminar flames [4,42] showed that the flame area evolved nonlinearly with increase in amplitude. In a recent work [43], it was shown that the cyclic flame surface destruction during the neighbouring flame front interaction was an important mechanism in self-excited oscillations. Lieuwen and co-workers [44] suggest a similar kinematic restoration process as a possible mechanism for nonlinear response of flame.

It is clear that various possibilities exist as to the origin of a flame's nonlinear response and that various techniques, with different associated uncertainties, are available for measuring the heat release rate that determines this nonlinear response. In an effort to understand this phenomenon better, in this paper, a relatively simple turbulent premixed flame was forced at high amplitudes and its response was quantified by chemiluminescence, FSD, and direct local heat release imaging (RX). The results provide both a comparison on the heat release measurements and some data on nonlinearity. The main objectives of the present paper are therefore: (i) to compare the various techniques for estimating the heat release rate and to apply them to an acoustically forced premixed flame stabilised by a bluff body; (ii) to explore how the flame response measured by these techniques behaves as a function of large excitation amplitudes; and (iii) to understand the origin of the phenomenon of saturation of the heat release response of premixed flames. The rest of this paper is organised as follows: the burner and the measurement techniques used are described in Section 2, while the results are presented and discussed in Section 3. The paper closes with a summary of the most important conclusions.

2. Experimental methods

2.1. Burner

A 10 kW acoustically excited bluff-body combustor was used during the current study. Fig. 1 shows the schematic of the burner assembly. The burner consists of a 300-mm-long circular duct of inner diameter (i.d.) 35 mm with a conical bluff body of diameter
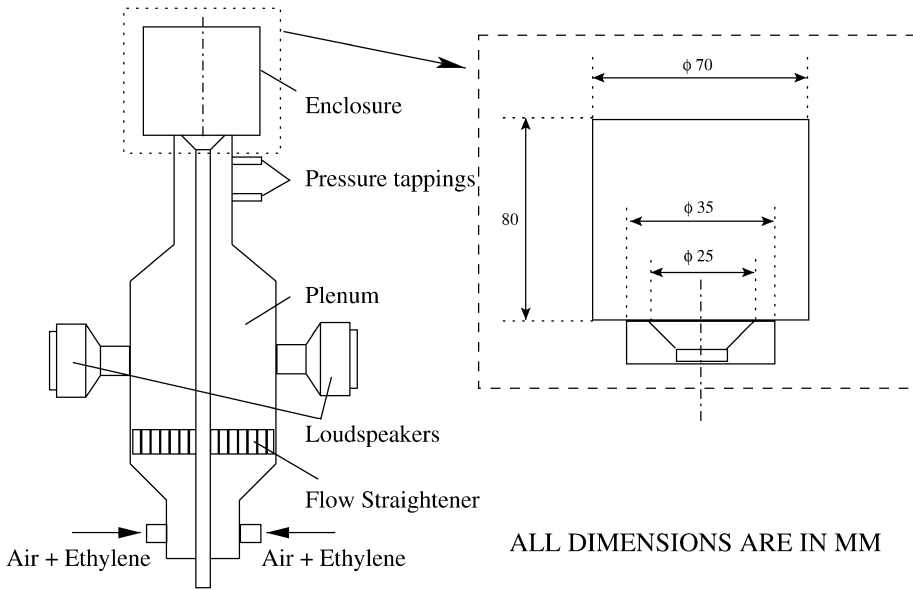
Fig. 1. Schematic of the burner.

25 mm giving a blockage ratio of 50%, which stabilises the flame. The burner duct houses pressure taps for acoustic pressure measurements. The premixed reactants flow through a 200-mm-long plenum chamber of inner diameter 100 mm. For the present work, ethylene was fully premixed with the air upstream of the burner. To introduce velocity oscillations at the bluff body, two loudspeakers were used. These speakers were mounted diametrically opposite to each other on the circumference of the plenum chamber. The loudspeakers were excited by a sinusoidal signal, generated using a TTi 40 MHz arbitrary waveform generator. The forcing amplitude (peak-to-peak voltage to the speakers) and the frequency of forcing were varied independently to understand the dependence of flame response on amplitude and frequency of forcing. The forcing achieved was as high as 80% of the mean velocity (i.e., $A = 0.8$) for certain forcing frequencies.

The flame was enclosed using a 80-mm-long fused silica quartz cylinder of inner diameter 70 mm which provided optical access for the imaging and also avoided equivalence ratio (ϕ) variations due to possible air entrainment from the surroundings. In order to reduce the interference from the acoustics of the downstream geometry on upstream forcing, the length of the enclosure was chosen to be small so that its resonant frequency was much higher than the frequency of forcing. For the present study, the forcing frequency was varied between 20 and 400 Hz while the fundamental frequency of the downstream duct is around 1000 Hz; hence, the resonant effects of the downstream geometry are minimised. Turbulent premixed flames of equivalence ratios in the range 0.55–

0.7 were used, with a bulk velocity of 9.9 m/s at the combustor inlet, giving a Reynolds number of approximately 19,000.

2.2. Measurement techniques

2.2.1. Acoustic and flow-rate measurements

The mass-flow rates of air and the fuel were measured and controlled using Bronkhorst Hi-Tech mass-flow controllers with measurement ranges of 12–600 litres per minute (lpm) for air and 1.2–60 lpm for ethylene, with an accuracy of ±0.5% of the full-scale deflection. Three Kulite high-sensitivity pressure transducers (Model XCS-093 with sensitivities of 4.2857×10^{-3} mV/Pa) were used to measure pressure perturbations and the two-microphone technique reviewed in [45] was used to determine the bulk velocity fluctuations at the combustor inlet from the pressure measurements. Direct measurements of velocity fluctuations were performed under cold-flow conditions with a Dantec hot-wire anemometer located at a radial distance of 15 mm from the bluff body centre to calibrate the two-microphone technique. The signals from the transducers and the hot-wire anemometer were amplified, digitised, and saved using a digital data acquisition system (National Instruments PCI 6034E, resolution 16 bits, input range 10 ± 0.05 V, maximum sampling rate 200 kHz). Data were acquired at a sampling rate of 10,000 Hz and time series lasting 2 s were collected and stored for postprocessing which resulted in a frequency resolution of 0.5 Hz.
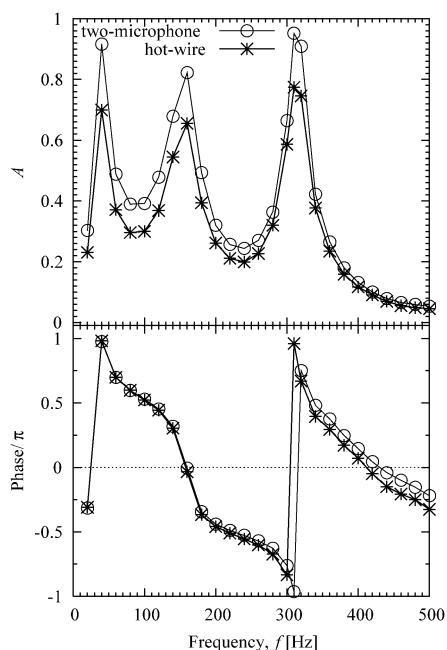
Fig. 2. Comparison of amplitude and the phase of the velocity fluctuation measured by the two-microphone method and a hot wire located at a radial location 15 mm from the bluff body under cold flow conditions, as a function of forcing frequency for a constant peak-to-peak input voltage to the speakers. $\langle U \rangle = 9.9$ m/s.

Fig. 2 shows the A values that can be obtained by the external excitation using an input signal of constant peak-to-peak voltage value, as a function of forcing frequency, and Fig. 2 also shows the phase difference (normalised using π), with reference to the forcing signal. These results suggest that the combustor plenum chamber with the air supply line acts like a resonator with peak responses around 40, 160, and 320 Hz, respectively, thus resulting in high A values around these frequencies. The first peak corresponded to the eigenmode of the combustor including the plenum and the air supply line, while the other frequencies were that of the geometric modes of the combustor including the plenum chamber. It can be seen from Fig. 2 that the two-microphone method slightly overestimates the magnitude of the velocity fluctuation but the trend of the variation is captured well. This discrepancy is due to the fact that in the two-microphone calculations an area-averaged velocity was used. Similarly, the phase of the velocity fluctuations relative to the input forcing signal is very similar from both techniques. Despite the good agreement, the two-microphone estimate was corrected based on the hot-wire measurement under the cold-flow conditions to provide accurate velocity fluctuation amplitude for characterisation of the hot-flow condition.
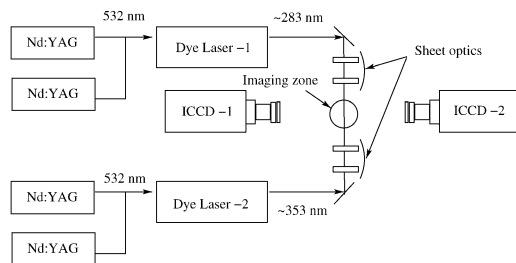

Fig. 3. Schematic of the laser layout used for simultaneous OH, CH_2O, and OH* imaging.

2.2.2. Simultaneous OH, CH_2O PLIF imaging

Fig. 3 shows the layout of the laser diagnostic facility used to measure heat release rate for the present study. The technique is described in more detail in Ref. [46]. The laser system consists of a cluster of 4 Nd:YAG lasers (Continuum Surelite), 2 dye lasers (Sirah Cobra-Stretch), and 2 high-resolution double-pulsed ICCD cameras (Lavision Nanostar). For OH PLIF, the frequency-doubled output from one dye laser (marked as Dye laser -1 in Fig. 3) was tuned near 283 nm to pump the $Q_1(4.5)$ transition of the $A^1\sum - X^2\prod(1,0)$ band. OH fluorescence from the $(0,0)$ and $(1,1)$ bands near 310 nm was captured on the ICCD camera (labelled ICCD-1 in Fig. 3) fitted with a UV f/4.5 Nikkor lens and a combination of UG 11 and WG 305 Schott glass filters. For CH_2O LIF excitation, the frequency-doubled output from the second dye laser (marked Dye laser-2) was tuned to pump the band $\tilde{A}^1 A_2 - \tilde{X}^1 A_1 4_0^1$ of CH_2O near 353 nm. The two counter-propagating laser beams were formed into overlapping sheets of 55 mm width, which intersected the axis of the bluff-body burner. The thickness of the laser sheet, defined as twice the distance from the centre of the beam to where the light intensity dropped to $1/e^2$ of its maximum value, was measured by the scanning knife-edge technique [47] and it was found to be 0.1 mm at the focal point (burner axis), increasing to not more than 0.2 mm at the confinement radius.

The CH_2O fluorescence was recorded on the other ICCD camera (i.e., ICCD-2) fitted with an f/1.2 Nikkor camera lens and filters (GG 375 (Schott) and 550 nm short pass), which provided broadband collection of the LIF signal and rejected out-of-band interference. The lasers were tuned off resonance to verify that the laser-generated interference was not an issue. The temporal separation of the laser pulses ensured that there was no cross talk between the two LIF measurements. In order to investigate local heat release fluctuations, the measurements were performed with a projected pixel resolution of 35 μm per pixel. For the FSD estimation, the OH LIF signals were recorded with a projected pixel size of 50–70 μm,

which was enough to give both high resolution and large imaging areas so that the whole flame was viewed.

Numerical results have established an excellent correlation of HCO production rate with heat release and burning rates in N_2-diluted premixed methane/air flames [34,36,37]. The major pathways leading to the production of CO and CO_2 in the lean combustion of hydrocarbon fuels proceed via HCO [34] through the reaction:

$$CH_2O + OH \rightarrow HCO + H_2O. \qquad (2)$$

The forward rate of reaction (2) can be written as $k(T)[CH_2O][OH]$, where k is the rate constant, T is temperature, and [ ] denotes number density. Since LIF signals are related to species densities, this provides an avenue to measure the reaction rate via the concentrations of CH_2O and OH. However, LIF intensities depend also on the temperature through the collisional quenching and the Boltzmann population fraction [34]. The product of simultaneously recorded LIF signals of CH_2O and OH can therefore be expressed as

$$(CH_2O \text{ LIF})(OH \text{ LIF}) \propto f(T)[CH_2O][OH]. \qquad (3)$$

Over a limited range of temperatures, it is possible to select transition lines such that $f(T)$ closely mimics the forward reaction rate $k(T)$ in Eq. (2) [34]. The excitation lines chosen during this work are the same as that of Refs. [33,34], which satisfy this criterion.

In atmospheric flames the fluorescence quantum yield is dominated by the quenching rates. In the case of OH PLIF, from judicious choice of excitation and detection wavelengths, the temperature dependence can be cancelled out and thus the PLIF images would essentially represent mole fractions [34]. However, with CH_2O molecules, there is a strong temperature dependence from the Boltzmann fraction. This temperature dependence was modelled in Ref. [34] and the formaldehyde LIF signal was represented by $(CH_2O \text{ LIF}) \propto X_{CH_2O}T^{-\beta}$, where X denotes mole fraction, with $2.2 < \beta < 3$ over the temperature range 800–1800 K; thus, the functional dependence for $f(T)$ [Eq. (2)] is between $T^{-0.2}$ and T^{-1}. In Ref. [34] it was shown that in the range of temperatures expected in the region of overlap of the OH and CH_2O, the primary dependence in the product of LIF signals is through the product of number densities. Thus, the product of the two LIF signals provided a measure of a quantity that correlated with local heat release rate. In the present study, an approach similar to that of [33–35] was followed; i.e., the product of LIF signals of OH and CH_2O was used to obtain a quantity which correlates with the heat release rate.

Despite the fact that the numerical study in Ref. [34] was performed for methane, the same conclusion applies to ethylene that gives higher quantities of CH_2O and hence better signal to noise ratios. Steady laminar flame calculations also indicate that this reaction contributes significantly to the heat release in a lean premixed ethylene/air flame [46], which suggests that the simultaneous OH and CH_2O technique should be applicable also to the ethylene flames used here. In a recent work [36], it was shown that the measurements from this technique in a laminar counterflow premixed flame of propane were in good agreement with computations with detailed chemistry, hence giving extra credence to the technique.

The laser imaging was phase locked with the reference signal. The TTL component of the forcing signal (the reference signal) triggered the CH_2O laser. After a delay of 500 ns, the OH laser was subsequently triggered. With respect to the flow and combustion time scales, this delay renders the laser measurements quasi-instantaneous. Both OH and CH_2O fluorescence signals were captured with the respective image intensifiers gated at 350 ns. The acoustic cycle was divided into 18 phases and at every phase angle 75–100 images were taken and saved for postprocessing and statistical analysis. The stored instantaneous images were processed and then averaged to obtain phase-averaged quantities (more details given later).

2.2.3. OH* and CH* chemiluminescence measurements

The photomultiplier tubes (PMT) used to measure the global OH* and CH* chemiluminescence during the present work were Hamamatsu (R3788) side-on PMTs, both fitted with interference filters of 10-nm bandwidth centred at 307 and 435 nm, respectively. The signal collection optics used for OH* and CH* chemiluminescence measurement were identical and were designed to collect light from the entire combustion zone and it was ensured that both the PMTs viewed the same region. The PMT measurements were recorded simultaneously with the acoustic pressure measurements using the data acquisition system described earlier. During the current study, along with the PLIF images, the OH* chemiluminescence was also recorded simultaneously by using the double-frame, double-exposure option of the ICCD-1 camera (Fig. 3), for which the intensifier was gated at 50 μs. The collection wavelength of OH* chemiluminescence images taken with the camera was broad (from 305 to 400 nm), while that of PMT measurements was a 10-nm-wide band around 307 nm.
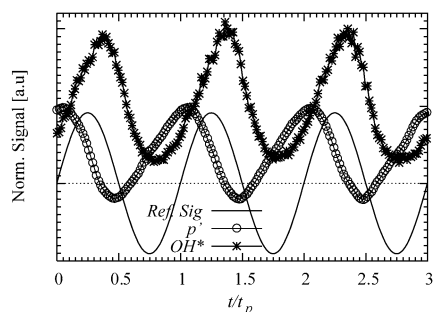
Fig. 4. Time series of normalised reference signal, acoustic pressure, and OH* chemiluminescence signal. Conditions are: $\langle U \rangle = 9.9$ m/s, $\phi = 0.55$, $f = 160$ Hz, and $A = 0.45$.

2.2.4. Time-resolved OH PLIF measurements

For the time-resolved OH PLIF measurements both dye lasers (1 and 2 in Fig. 3) were tuned near 283 nm to pump the $Q_1(6)$ transition of the $A^1 \sum - X^2 \prod (1, 0)$ band. The four Nd:YAG lasers which pumped these dye lasers were triggered in sequence at a time interval of 1 ms. The images were captured using the double-frame, double-exposure option of the cameras resulting in four OH PLIF images separated by 1 ms. This duration is not short enough to tract the quickest transients of the turbulent flame. For example, using an advection speed of about 10 m/s, 1 ms gives a distance of 10 mm, which is about half a bluff-body diameter. However, some very useful insights can still be drawn on the dynamics of larger scale structures, as will become evident later.

2.3. Determination of the flame response

2.3.1. Based on OH* and CH* chemiluminescence

Fig. 4 shows an example time series of simultaneously performed reference signal, acoustic pressure, and OH* chemiluminescence measurements. Such traces were analysed spectrally for different forcing frequencies and amplitudes using the fast Fourier transform (FFT) technique. From such power spectra, the complex amplitude of the quantities $OH^{*\prime}$ and $CH^{*\prime}$ at the forcing frequency f, were determined. These values were normalised using the time mean values of OH* and CH*, respectively, to obtain $OH^{*\prime}(f)/\langle OH^* \rangle$ and $CH^{*\prime}(f)/\langle CH \rangle$, which are used as estimates of $Q'(f)/\langle Q \rangle$. The two quantities, $Q'(f)/\langle Q \rangle$ and $u'(f)/\langle U \rangle$ determined from the simultaneous acoustic pressure measurements using the two-microphone method, were used to determine the flame transfer function $H(f, A)$ defined by Eq. (1).

2.3.2. Based on flame surface density

The phase-locked instantaneous OH PLIF images were used to estimate the flame surface density. The OH PLIF intensity images were corrected for the

background noise and also for the beam profile inhomogeneities. These images were then filtered with a Gaussian filter of width 3 pixels to remove the high-frequency noise. The filtered intensity images were subsequently resized by 2×2 binning, which resulted in a projected pixel size of 150 μm and were then converted into binary images by an intensity thresholding procedure. Here, the pixel value of 1 corresponds to progress variable equal to 1 (burnt gases) and pixel values of zero indicate progress variable 0 (fresh mixture). The instantaneous flame contour was obtained from the instantaneous map of progress variable. The flame surface density (FSD) was computed with a procedure similar to the one noted in Ref. [30]. The interrogation box dimension chosen for the FSD computations was 0.5×0.5 mm. The dependence of box size on the FSD computation was investigated as noted in Ref. [48] and it was found that the results were independent of the box size for the chosen values during these computations.

Fig. 5a (i) shows a typical instantaneous OH PLIF image and the corresponding instantaneous flame trace (image (iv) in the sequence). By averaging the instantaneous progress variable and flame surface density images taken at the same phase, phase-averaged progress variables and phase-averaged flame surface density images are obtained. In order to compare the evaluated quantity with measured global heat release measurements, such 2D FSD phase-averaged images were revolved around the central burner axis to obtain a 3D surface. The axisymmetric assumption was verified by horizontal OH PLIF measurements performed on an open flame under similar flow conditions. This phase-averaged quantity obtained for every phase over the full cycle at each forcing condition was used to compare with the corresponding quantity determined from chemiluminescence. Despite the fact that the flame surface area estimate obtained in this way may differ from the true flame surface area due to the presence of fine scale wrinkles along the flame circumference in turbulent flames, the flame surface area fluctuations reported in [23] were found to correlate well with CO_2^* chemiluminescence.

2.3.3. Reaction rate evaluation based on OH and CH_2O PLIF

In order to obtain heat release rate from the OH and CH_2O PLIF images, a number of corrections were made on the raw fluorescence images. As noted earlier, the images were corrected first for the background noise. Secondly, images were corrected for the beam profile variations. Finally, both OH and CH_2O images were overlapped on a pixel-by-pixel basis. In order to do this, a target image was aligned in the measurement plane defined by the laser sheets and in the field of view of both cameras. From the coordinates
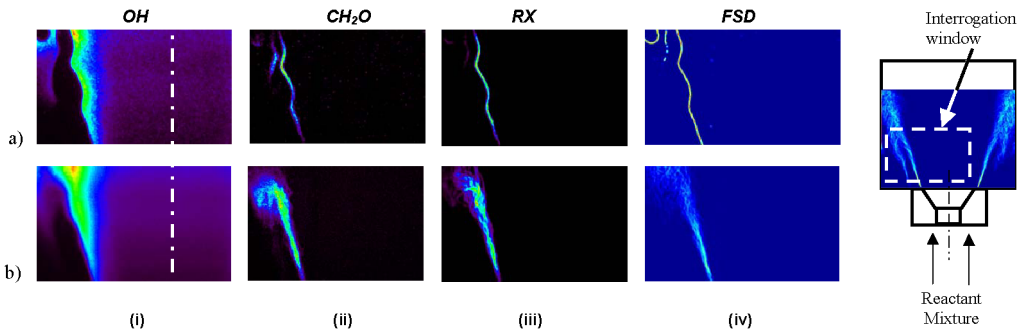
Fig. 5. Simultaneous instantaneous (a) and time-averaged (b) images of OH, CH$_2$O, and the heat release rate (RX) and flame contour. (The field of view is 40×36 mm, lower side of image is 10 mm above the bluff body.)

of the target images, polynomial warping coefficients were extracted and used to geometrically transform one of the images to overlap with the other [46]. The precision of the image matching was in the subpixel range. The corrected images were resized by 2×2 binning, which resulted in an effective spatial resolution of 100 μm and then multiplied on a pixel-by-pixel basis to obtain the local heat release image.

Fig. 5a (ii) shows a typical instantaneous CH$_2$O image and the reaction rate (RX) image (iii) along with the corresponding flame trace determined from the OH image (iv). These instantaneous images were averaged to obtain time-averaged reaction rate image shown in Fig. 5b to indicate the width of the flame brush in this unforced flame. Fig. 5b shows typical time-averaged distributions of OH, CH$_2$O, and heat release rate along with their flame brush. From these images it can be seen that the flame contour obtained from OH PLIF essentially marks the flame, while the reaction rate imaging technique has also captured the local heat release variation along the flame.

2.4. Error estimates

The uncertainties in the values of heat release fluctuations Q' over the mean value $\langle Q \rangle$ arise from many sources. First, there is broadening due to the FFT processing, which is estimated to cause an uncertainty of about 0.1% in the reported $Q'/\langle Q \rangle$. Secondly, there is statistical uncertainty due to the finite number of samples taken for all techniques. This is estimated to be around 0.4% for the PMT data, 10% for the FSD, and 15% for the heat release imaging. Thirdly, reproducibility of the whole system (e.g., setting of flow rates, forcing, alignment of optics, etc.) was checked by performing identical experiments on different dates and it was found that $Q'/\langle Q \rangle$ was different by not more than 1% for the PMT data and 10% for the FSD. Hence these can be used as final estimates of the accuracy of these techniques for the relative magnitude of heat release fluctuations.

The heat release imaging technique has not been used in a fully quantitative manner yet and it is difficult to estimate its precision. Uncertainties in the simultaneous OH and CH$_2$O PLIF may arise due to variation in the quenching cross sections through temperature dependence. It was reported in Ref. [49] that the calculated error in quantum yield in the temperature range where OH can be detected could be as high as $\pm35\%$. These uncertainties do not affect the FSD calculation, which relies only in the large difference between OH in the unburnt and the burnt gases. No quenching data are available for CH$_2$O and hence such corrections are not possible. Hence, the RX measurements in this paper are not quantitative, as also suggested by [36]. Despite this, measurements in laminar premixed flames [46] show that the heat release as a function of equivalence ratio, divided by the corresponding measurement at $\phi = 1$, has a trend to within 20% of laminar flame computations. The reaction rate along turbulent premixed flames as a function of local flame curvature, normalised by the reaction rate at no curvature, also followed the expected trend from direct numerical simulations [46], with the reaction rate decreasing as the flame switched from negative to positive curvatures. This shows that the RX technique produces reasonable results concerning the local heat release rate, if the data are suitably normalised. In this paper, we use the RX data only for the ratio $Q'/\langle Q \rangle$, which should not be affected by these uncertainties.

3. Results and discussion

The measurement techniques presented in the previous section were used to measure the heat release response of forced lean premixed flames. In this section, a comparison of the heat release rate evaluated from these techniques is presented. Furthermore, the dynamics of the local flame structure and the nonlinear response of the flames to forcing are elucidated
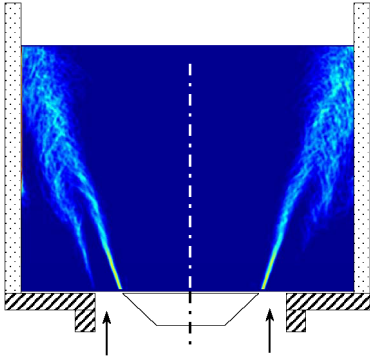
Fig. 6. Time-averaged FSD image of an unforced flame. Conditions are: $\phi = 0.55$, $\langle U \rangle$ of 9.9 m/s. (The field of view is 70×55 mm, lower side of image is 0.5 mm above the bluff body.)

in detail. Finally, this section closes with a discussion about the mechanism of heat release modulation and the origin of saturation in forced premixed flames.

3.1. Dynamics of the forced flame

Fig. 6 shows a typical time-averaged FSD image of an unforced flame. The image shows that the flame was primarily anchored at the shear layer generated by the bluff body, with some flame elements at the outer shear layer generated by the rearward facing step (dump plane). Due to lower local temperatures in the outer recirculation caused by the dump plane, stabilisation of such flame elements was not achieved. When the reactant mixtures were forced with sufficiently large amplitude, these shear layers rollup to form a counterrotating vortex pair [50]. The inner shear layer rolls inward and the outer shear layer rolls outward. Fig. 7 shows the evolution of the flame using phase averages of FSD when the flame was forced at 160 Hz (a condition selected to give high A value,

from Fig. 2) with the value of forcing amplitude, A, equal to 0.64, a relatively high value. The 18 images show the flame surface evolution at every $20°$ phase angle. The image sequence shows clearly the deformation of the flame base and later resulting in roll up of the flame front stabilised at the inner shear layer, radially inward while the flame stabilised on the outer layer rolled up outward. It can be observed that the rolled-up flame front grew in size and was convected with the flow and impinged on the wall. Once this disturbance moved out of the imaging region, a new vortex started forming at the base of the flame. This phenomenon was cyclic following the imposed velocity fluctuations. The phase-averaged FSD images obtained from these PLIF images were revolved around the burner central axis and were used to obtain the normalised cyclic heat release fluctuation and this was compared with the quantity obtained from OH* chemiluminescence imaging.

Fig. 8 shows the heat release variation evaluated from spatial integration of each of the phase-averaged FSD images in Fig. 7 and the OH* chemiluminescence images captured simultaneously during the experiments. From Figs. 7 and 8, it can be noted that the heat release decreased with the beginning of the rollup and decreased further to attain the lowest value around 100–$120°$, which corresponded to the case where the flame surface area was at the lowest value due to the vortex rollup. The vortex while moving downstream toward the wall increased in size, increasing the flame area. The heat release evaluated from these measurements increased during this phase to attain a peak value around $280°$, which corresponded to the highest flame surface area.

The heat release variations captured by both FSD and OH* are in agreement with a small difference in magnitude and phase. The agreement between FSD and chemiluminescence was noted earlier by [32]. It was observed that the difference in the magnitude
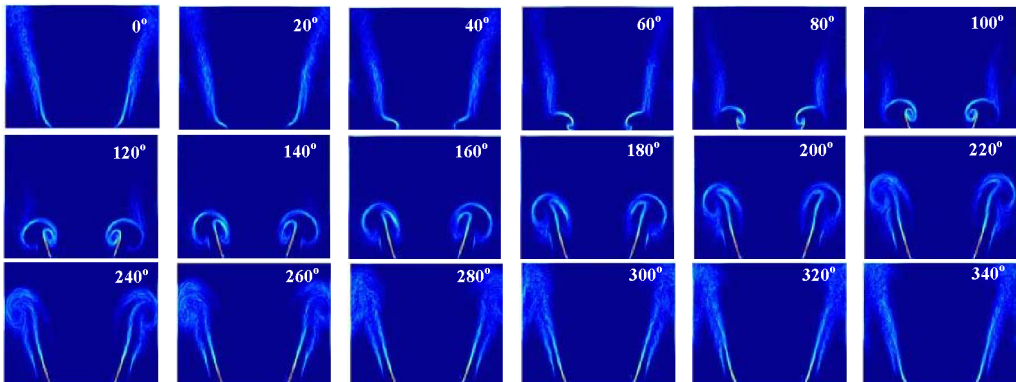

Fig. 7. Phase-averaged FSD image sequence under strong acoustic forcing: $\langle U \rangle = 9.9$ m/s, $f = 160$ Hz, $A = 0.64$, $\phi = 0.55$.
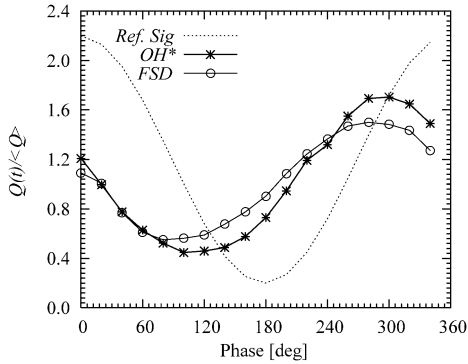
Fig. 8. Comparison of the global heat release fluctuations evaluated from phase-averaged FSD and from OH* chemiluminescence images (both imaged simultaneously, with estimated resolution of 50 μm): $\langle U \rangle = 9.9$ m/s, $\phi = 0.55$, $f = 160$ Hz, and $A = 0.64$.

between the two measurement techniques increased with increase in forcing amplitude, but was about 20% at the most. These measurements suggest that the FSD can capture the global heat release variation well despite the reservation of it being a planar measurement and that the flame speed can vary along the flame.

The FSD technique was further compared with high-resolution heat release images under different forcing conditions in an effort to evaluate its accuracy. These experiments were performed to image the vortex-dominated region only. During these measurement cases, the forcing cycle was resolved into 13 phase bins and OH and CH_2O PLIF images were taken at every phase and stored. As described earlier, these instantaneous images were processed to obtain RX and FSD image and then these instantaneous images were averaged to obtain phase-averaged RX and FSD images, respectively. The heat release variation over the forcing cycle was obtained from these phase-averaged RX and FSD images. Figs. 9a and 9b

show typical instantaneous and phase-averaged distributions of OH, CH_2O, OH*, and the corresponding RX and FSD images, respectively. These images were phase-locked at a phase angle of 40° with reference to the forcing signal. It can be seen clearly that the flame, stabilised at the shear layers, has rolled up into a counterrotating vortex pair due to strong acoustic forcing. From the images it can also be seen that the FSD marked the flame very well, in full agreement with the RX imaging. However, the instantaneous RX image shows a smaller heat release at the vortex region formed at the outer shear layer (marked as A in Fig. 9) than at the flame region inside the bluff-body-generated recirculation zone (marked B in Fig. 9), something that an FSD-based heat release measurement cannot capture. The phase-averaged images reflect these facts clearly. It can also be observed from the instantaneous and averaged OH* images, despite longer integration times (50 μs), that the heat release was not captured well in the outer recirculation regions due to weaker emissions from these regions. Both OH* and RX images show higher heat release in the region A marked in Fig. 9. This is due to fact that the acoustically excited inner shear layer when rolled into a vortex brought reactants between the flame surfaces resulting in higher heat release at the point of focus.

We should finally note that even at high forcing amplitudes, the RX imaging always showed a connected reaction zone without any evidence of localised extinctions, which may have been expected because the images cover the vortex-dominated region close to the bluff body where high strain rates are possible. The absence of localised extinctions seems to suggest that this is not a key mechanism determining the flame response in this flow.

Fig. 10 shows the cyclic evolution of heat release directly evaluated from RX imaging and that estimated from the FSD, for the case presented in Fig. 9. It can be clearly seen from this figure that when the
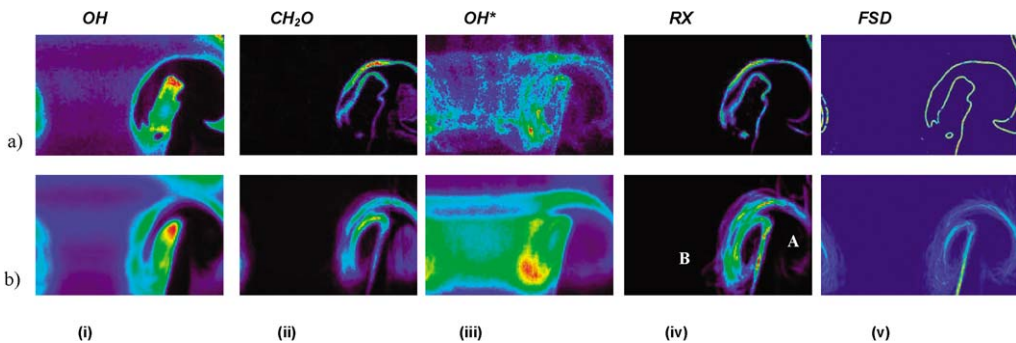

Fig. 9. Simultaneous instantaneous (a) and phase-averaged (b) images of OH, CH_2O, the heat release rate (RX), and flame contour at 40° phase angle with reference to the forcing signal: $\langle U \rangle = 9.9$ m/s, $\phi = 0.55$, $f = 160$ Hz, and $A = 0.64$.
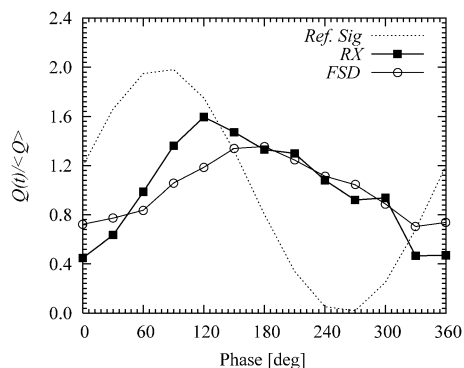
Fig. 10. Comparison of the heat release fluctuations evaluated from phase-averaged RX and FSD images: $\langle U \rangle =$ 9.9 m/s, $\phi = 0.55$, $f = 160$ Hz, and $A = 0.64$.

vortex appeared, the heat release evaluated from both the measurements increased, but the heat release evaluated from RX peaked ahead of that computed from FSD. The magnitude of heat release fluctuation over its mean evaluated from RX is around 10–15% higher than that evaluated from the FSD technique and this difference increased up to 20% with increase in forcing amplitude. The increase in local heat release rate captured by both techniques in the vortex-dominated region and the fact that global heat release decreased with the appearance of the vortex (Fig. 8) suggest that the flame annihilation in the regions above the vortex region could be playing a significant role in heat release modulation.

It must be noted that the accuracy of the RX imaging is critically dependent on the geometrical transformation procedure. Hence, the RX imaging technique if used to image a larger interrogation window must be interpreted with care due to the increased error in estimations. The error in FSD estimates is mainly due to the noise in the images. The fact that the FSD in the current study is based on OH PLIF, which has a high signal to noise ratio, makes FSD a better choice for determination of local mean reaction rate while performing global imaging (i.e., bigger interrogation window size).

Figs. 8 and 10 suggest that FSD underestimates the heat release rate by not more than 20% at the highest forcing amplitudes. This difference may be attributed to the burning rate fluctuations along the flame as seen in Fig. 5a (iii) and Fig. 9a (iv), although we cannot be certain at this stage as the RX technique is not fully quantitative. We can conclude, however, that tracking the evolution of the flame front with FSD and measuring global chemiluminescence are probably sufficient tools to understand flame response even at high amplitudes. Details on the nonlinear response are given next.

3.2. Nonlinear amplitude dependence of the flame response

Fig. 11a shows the dependence of the OH* and CH* chemiluminescence upon the inlet forcing amplitude at the same forcing frequency. It can be clearly seen from the figure that the heat release response saturates at an amplitude of around 15% marked as x in the figure. With further increase in amplitude the flame response levelled off which is marked as x'. Fig. 11c shows the transfer function (i.e., the y axis of Fig. 11a divided by A) and the corresponding phase information calculated from the data presented in Fig. 11a. A linear response would be a straight horizontal line. The transfer function measurements show clearly a nonlinear amplitude dependence: at lower amplitudes the transfer function drops rapidly with increase in amplitude and once the magnitude reached a certain value, with further increase in amplitude there was little change in transfer function. At the point corresponding to x', the transfer function again starts decreasing. It can be seen from Fig. 11c that the phase of the transfer function was nearly independent of the amplitude of forcing up to the point x, after which the phase increased with increasing forcing amplitude. From these data it is also clearly evident that the magnitude and phase of the heat release response measured by both OH* and CH* chemiluminescence techniques are in good agreement. Bellows and co-workers [38,51] observed saturation similar to the x (marked in Fig. 11a) in their experiments with forced turbulent premixed flames. They speculated this saturation to be due to a nonlinear evolution of the flame surface area. However, they insisted on the need for optical measurements to confirm this, and such measurements are discussed below.

Fig. 11b shows the heat release response evaluated from FSD as a function of forcing amplitude. The figure shows two saturation points similar to that of OH* and CH* measurements. However, the magnitude of the normalised response measured from FSD technique has lower values compared to that of chemiluminescence measurements, which may be due to local burning rate fluctuations along the flame contour. These measurements confirmed that the level of contribution of flame surface modulation to the total heat release response is significant and flame area evolution is playing a key role in the observed saturation. This is consistent with results obtained by Schuller et al. [6] for laminar flames.

Fig. 12 shows averaged FSD images for the same case presented in Fig. 11 at a particular phase angle (120° w.r.t. forcing signal), at different forcing amplitudes. It can be seen that as A increases from 0.23 (corresponding to point x marked in the Fig. 11) the flame surface is increasingly curved. It can also be
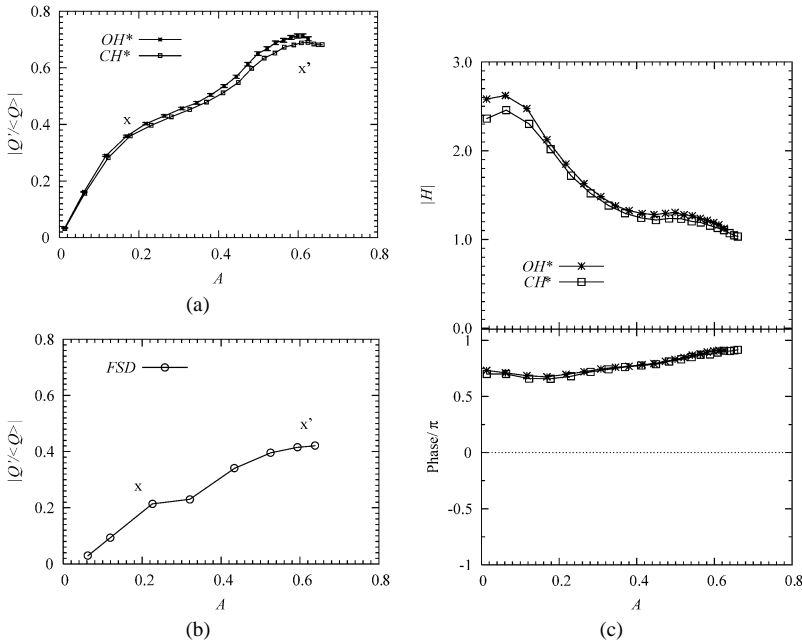
Fig. 11. The dependence of normalised global heat release fluctuation upon the forcing velocity amplitude A for a forcing frequency $f = 160$ Hz, measured using OH* and CH* chemiluminescence (a) and evaluated using FSD (b). (c) The magnitude of the transfer function [Eq. (1)] and its phase evaluated from the data of (a). (x and x' denote the points of saturation, discussed in detail in the text.)
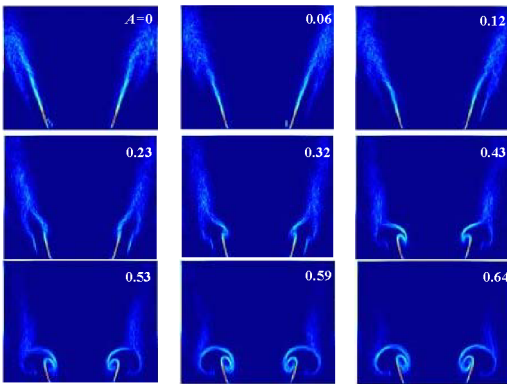

Fig. 12. Phase-averaged FSD images at $120°$ relative to the reference signal for different values of A. Conditions are: $\langle U \rangle = 9.9$ m/s, $\phi = 0.55$, and $f = 160$ Hz.

seen that the vortex rollup has shortened the flame, which in turn reduced the total flame area nonlinearly, despite the fact that the flame area is expected to be increased by flame elements wrapping around the vortex. It can be observed from these images that the intensity of the flame elements above the vortex region decreases with increase in amplitude of forcing, suggesting possible flame surface destructions in these regions. Further increase in amplitude shows decreased response in FSD and it can be seen in Fig. 11b that the response levelled off around $A =$

0.59, marked as x'. It can be seen that the flames at $A = 0.59$ and 0.64 are virtually identical, which explains why the last two points in Fig. 11b show identical $Q'/\langle Q \rangle$.

The finite amplitude response of the flame was investigated further for different forcing frequencies between 20 and 400 Hz. However, only three frequencies other than 160 Hz are presented here, selected so that they give relatively high magnitude of inlet forcing. Fig. 13a shows the amplitude dependence of heat release response of the flame at 40 Hz with the corresponding magnitude of transfer function and the phase information measured using OH* and CH* chemiluminescence. It is evident from the figure that the chemiluminescence response was linear throughout the forcing conditions. The magnitude of transfer function shows a nearly linear dependence on the amplitude while the phase seemed to be independent of the amplitude of forcing. During these measurements it was noted in PLIF images that there was no shear layer rollup, and the flame area modulation was only by the turbulent motion of the flame.

Figs. 13b and 13c show the amplitude dependence of the heat release response and the corresponding transfer function calculations when the flame was forced at 240 and 310 Hz. As in the case of 160 Hz forcing, the appearance of the saturation point x was consistent with the appearance of the flame rollup. However the amplitude of the saturation for 240 and
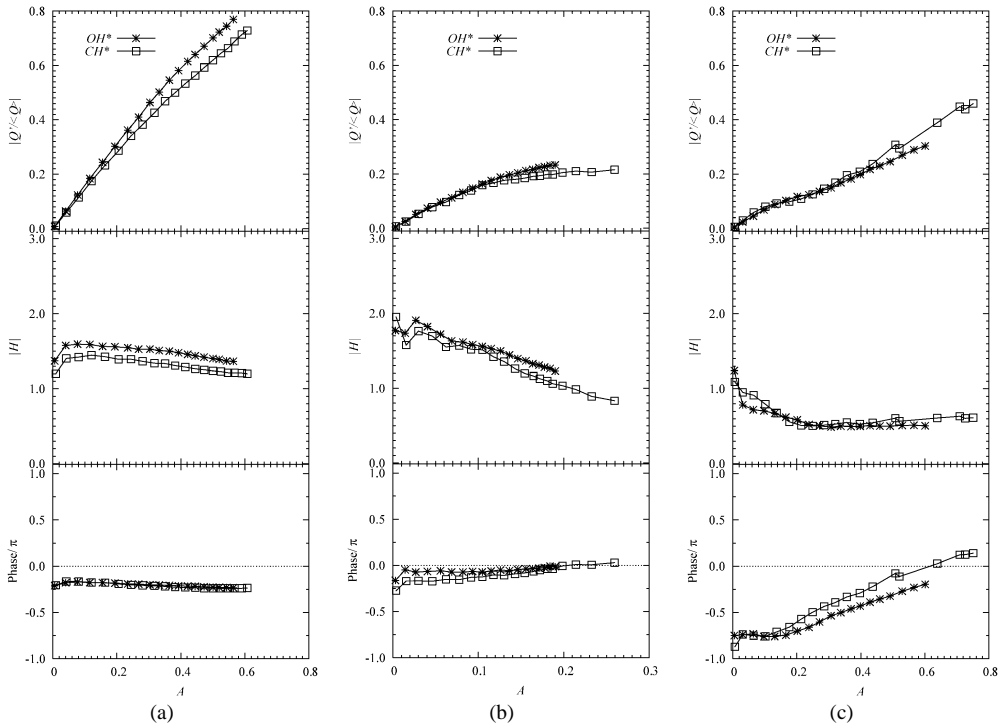
Fig. 13. The dependence of normalised global heat release fluctuation upon the forcing velocity amplitude A, measured using OH* and CH* chemiluminescence, and their corresponding transfer function and the phase relation for frequencies (a) 40 Hz, (b) 240 Hz, and (c) 310 Hz, respectively. For all, $\langle U \rangle = 9.9$ m/s, $\phi = 0.55$.

310 Hz forcing conditions was found to be lower than that of the 160 Hz forcing. This could be due to the fact that the amplitude of inlet oscillation required to achieve excitation of the shear layer to roll up into vortex has strong frequency dependence. It was shown in Ref. [14] that the required amplitude to excite the shear layer to roll up decreases with increasing frequency. It can also be seen that the phase dependence for forcing at 310 Hz has a linear dependence upon the amplitude up to the point of saturation, while beyond that point the phase increased with increase in forcing amplitude. This could be due to the fact that at this forcing frequency the flame might not be acoustically convectively compact. (A flame whose length is much less than an acoustic convective wavelength is referred to as acoustically convectively compact; see Ref. [7].) The optical measurements showed that for these cases (frequencies), before one vortex moves out of the combustion zone, a new vortex appeared at the base of the flame. The interaction of these two vortices could be causing this nonlinear dependence of phase on the amplitude.

In an effort to understand further the response of the flame to acoustic forcing, the transfer functions measured at different forcing frequencies for a range of amplitudes are consolidated in Fig. 14. Fig. 14a shows the magnitude of the transfer function at differ-

ent forcing frequencies for different amplitudes, and Fig. 14b shows the phase between the heat release and the velocity fluctuations. The magnitude of transfer function was found to decrease with increasing amplitude for all the forcing frequencies (better represented in Fig. 15). However, at lower frequency ranges this scatter was very low when compared to that of high-frequency forcing conditions.

The phase plot (Fig. 14b) shows the variation in phase of the transfer function as the function of forcing frequency, which suggests a definite time delay. This time delay was referred to as "fuel convection delay time" in Ref. [1]. From the data presented in Fig. 14b it was calculated to be of the order of 8 ms. This delay time along with the mean velocity of 9.9 m/s would translate into a convection distance of ~80 mm, which correspond to the length of the region of measurement. It can be observed from the figures that the phase measured above 280 Hz had more scatter than at the lower frequencies; this could be again due to the fact that the flame was not acoustically convectively compact. These are the conditions where the spread in time delay [52] must be modelled with care.

To better understand the effect of forcing amplitude on the frequency response of the flame, the data presented in Fig. 14 were reconstructed for constant amplitude of forcing from the interpolation between
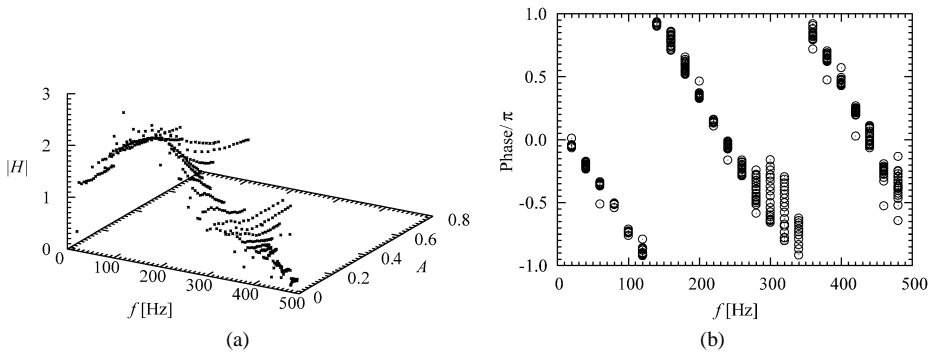
Fig. 14. (a) Flame transfer function as a function of frequency and amplitude and (b) the relative phase relation. $\langle U \rangle = 9.9$ m/s, $\phi = 0.55$.
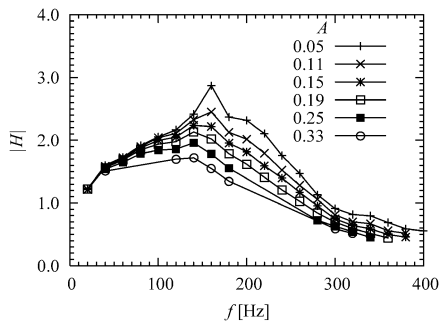

Fig. 15. Transfer function evaluated from the data of Fig. 14 using binomial curve-fit as a function of frequency for the indicated A.

the magnitude of transfer function and the amplitude of forcing for every frequency using a bilinear fit. Fig. 15 shows the reconstructed flame transfer function measurements for constant forcing amplitude. It can be observed that with increase in forcing amplitude the magnitude of the transfer function decreases, this decrease being greater for higher frequencies than for the lower frequencies. During these experiments, it was observed that up to nearly 100 Hz, there was no significant flame surface modification irrespective of the magnitude of the forcing amplitude. For the higher forcing frequencies, flame surface rollup was observed. Since this is amplitude dependent, significant difference in the amplitude dependence of the flame responses at low- and high-frequency forcing occurs.

3.3. Effect of equivalence ratio on nonlinear response

Fig. 16a shows the effect of equivalence ratio on the nonlinear heat release response of the flame forced at 160 Hz with different forcing amplitudes. The equivalence ratio was varied from 0.55 to 0.7 and the OH* chemiluminescence and acoustic pressure measurements were performed simultaneously to

obtain the global heat release response of the flame. Fig. 16b shows the magnitude of transfer function and phase for the case presented in Fig. 16a. As suggested earlier, the saturation was determined by the flame front rollup. The amplitude required for this rollup was higher for higher equivalence ratios possibly because the corresponding increase in laminar burning velocities shifts the flame position relative to the vortex. The phase of the transfer function was also found to increase with increase in equivalence ratio; however, the trend in variation as a function of amplitude was same for all cases.

It is interesting to also note that for the equivalence ratios 0.67 and 0.7 and after the saturation, an increase in amplitude of forcing resulted in sudden drop in heat release response, marked as x' in the figure. The time series measurement of OH* and the corresponding cold-flow velocity measurements before and after the point of saturation x' are shown in Figs. 17a and 17b, respectively. The velocity measurements show relatively small harmonic contents; however, the OH* clearly shows a disproportionately larger distortion of the waveform after the saturation, suggesting a strong response at a harmonic frequency. The amplitude required to obtain this saturation x' was also found to decrease with increase in equivalence ratio.

In order to better understand this nonlinear behaviour, the inlet velocity measurements were analysed to determine the amount of harmonic content under cold flow. It was observed that there was a linear increase in harmonic content during forcing (Fig. 18). However, the ratio of fluctuation of heat release at the first harmonic frequency to that of the forcing frequency showed a highly nonlinear variation against the forcing amplitude (see Fig. 19). For a particular equivalence ratio this relative response to the first harmonic frequency was found to increase linearly up to the saturation point x (marked in Figs. 16 and 19), after which this relative response stayed constant. This suggests that with the appearance of the flame rollup, the response to the harmonic frequency was suppressed.
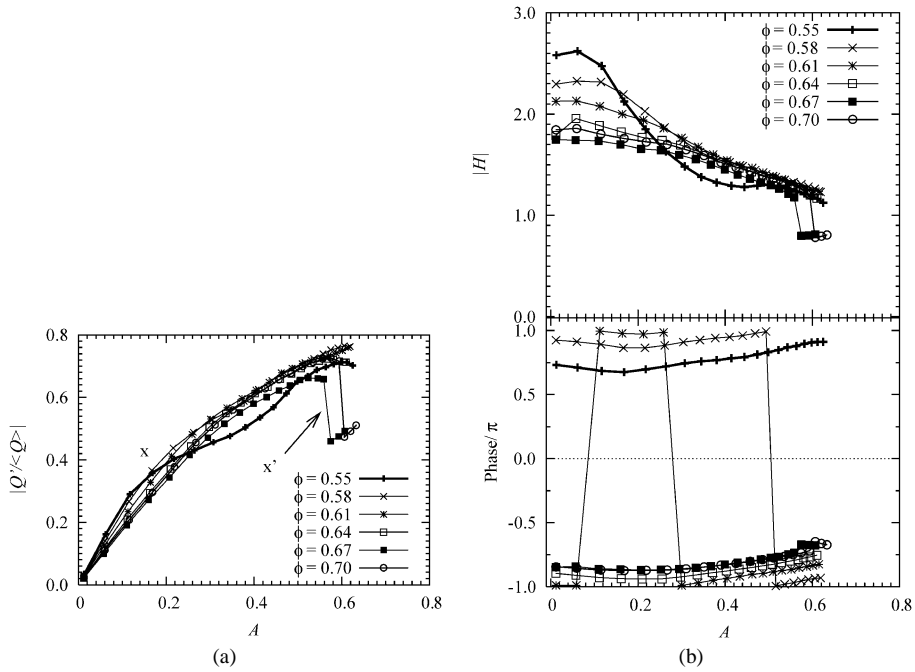
Fig. 16. (a) The normalised global heat release fluctuation measured as a function of A for various equivalence ratios, using OH* chemiluminescence. (b) The corresponding transfer function and the phase: $\langle U \rangle = 9.9$ m/s, $\phi = 0.55$ (x and x' are points of saturation, see text).
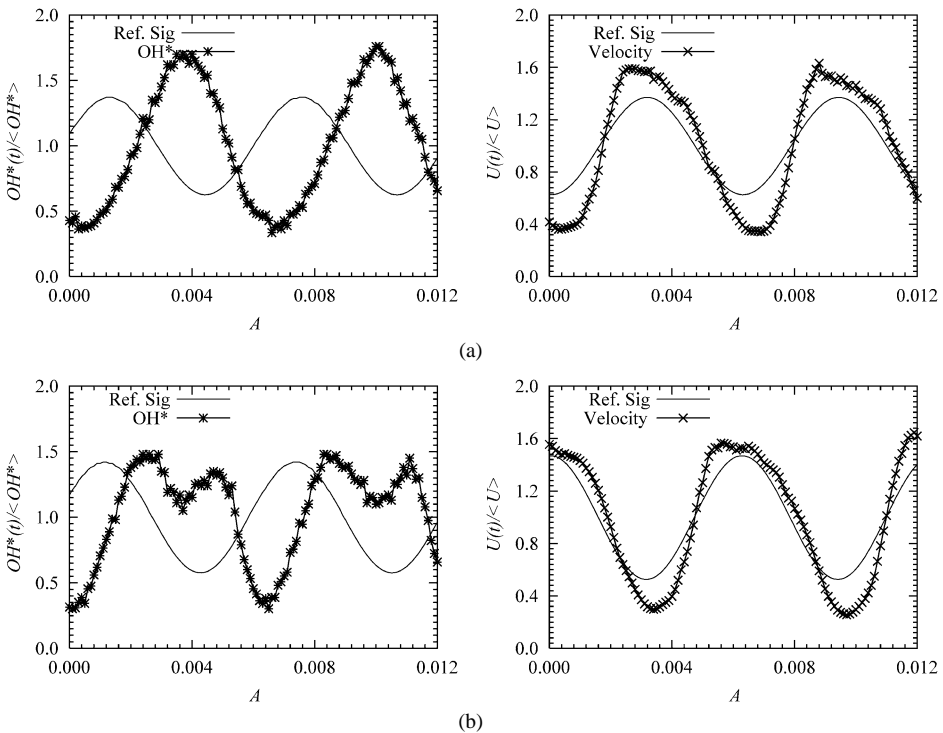

Fig. 17. Time series of OH* chemiluminescence and the corresponding cold flow inlet velocity measurements (a) before and (b) after saturation noted as x' in Fig. 16 with A values 0.57 and 0.64, respectively. $\langle U \rangle = 9.9$ m/s, $\phi = 0.67$, $f = 160$ Hz.
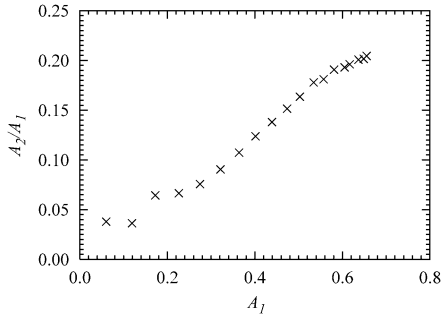
Fig. 18. Variation of ratio of amplitude of inlet velocity fluctuation at first harmonic of the forcing frequency (320 Hz) A_2, to that at the forcing frequency (160 Hz), A_1 upon amplitude. $\langle U \rangle = 9.9$ m/s.
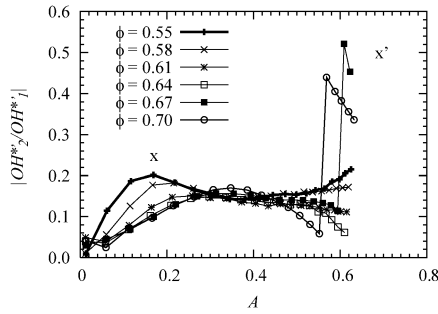

Fig. 19. Variation of ratio of amplitude of heat release fluctuation at first harmonic of the forcing frequency (320 Hz) to that at the forcing frequency (160 Hz) upon amplitude over different equivalence ratio: $\langle U \rangle = 9.9$ m/s (x and x' are points of saturation, marked in Fig. 16).

This proportional harmonic response increased suddenly with further increase in amplitude (for certain equivalence ratio conditions, here 0.67 and 0.7). This behaviour could be due to a complex interaction among flame, harmonic content present in the velocity, and the upstream geometry. An analysis of the response of laminar flames to monochromatic velocity forcing [6] also suggested that the flame surface fluctuations contained harmonics of the forcing frequencies. To understand this nonlinear flame response to multiple frequencies in inlet velocity fluctuations further detailed investigation with optical measurements is necessary. However, the present data suggest an additional reason why transfer functions can be nonlinear.

3.4. Discussion

In this paper, chemiluminescence measurements (from OH* and CH*), both measured continuously (using PMT) and by phase-averaged (using ICCD) imaging along with laser-based measurements, flame surface density (FSD) based on OH PLIF, and reac-

tion rate (RX) imaging based on simultaneous OH and CH_2O PLIF, were used to investigate the heat release modulation and to understand the nonlinear response of a turbulent premixed flame to high-amplitude inlet velocity fluctuations. The reaction rate (RX) imaging has been proved to correlate well for some hydrocarbon fuels (methane, propane, and ethylene) both computationally and experimentally for laminar flame under lean conditions [33,34,36,37]. However, the technique is yet to be used extensively as a quantitative measure of heat release. During the present study with turbulent fully premixed flames, the reaction rate imaging was found to capture the local heat release variation well in the vortex dominated regions, hence extending previous results from laminar flame–vortex interactions [33,34]. This suggests the potential of the technique in exploring combustion instability in the nonlinear regime where strain and curvature may play an important role. It has been found here that such local effects are not very large contributors to the global heat release modulation with the forcing.

The flame surface density (FSD) based on OH PLIF was found to agree well with chemiluminescence in Refs. [23,32] and also during the present study. Furthermore the FSD measurements agreed reasonably well with RX imaging. Apart from the fact that the FSD evaluation is less expensive compared to RX imaging, the data from the present study prove the ability of the FSD technique to capture the nonlinear heat release response of the flame. This implies certain confidence in using FSD in evaluating local mean reaction rate for fully premixed flames.

It was observed that the flame response measured using OH* and CH* is in very good agreement (Fig. 11). However, care must be taken while measuring CH* (which lies in visible region), due to possible interference from the ambient light. If this happens, it would result in higher mean signal, thereby affecting the magnitude of the transfer function greatly. During the present investigation, the OH* and CH* chemiluminescence measurements were found to capture the nonlinear flame response well. Furthermore the agreement between the techniques OH* and FSD and the later with RX imaging even in the vortex-dominated regime increases the confidence in chemiluminescence emission measurements.

For the transfer function measurement, estimating the global response is more critical than the local variation. The fact that the chemiluminescence technique is cheaper and requires no additional skills for computation or measurements and the ability to monitor fluctuations continuously in time make the chemiluminescence measurements a reasonably good choice of instrument. The chemiluminescence can also be used to evaluate heat release from imperfectly pre-
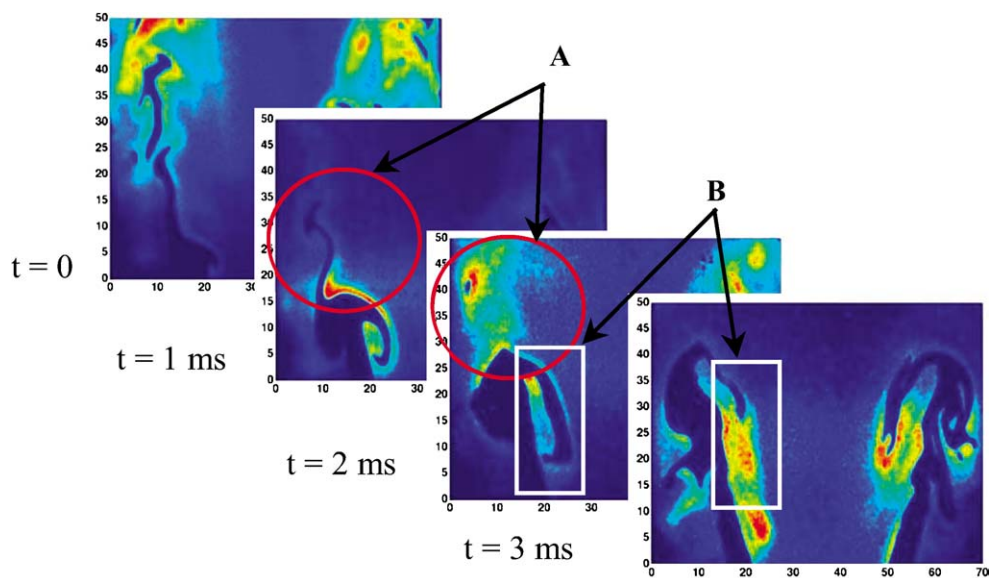
Fig. 20. Time-resolved OH PLIF images of a flame subjected to strong forcing showing flame annihilation events. A and B: $\langle U \rangle = 9.9$ m/s, $\phi = 0.55$, $f = 160$ Hz, $A \sim 0.5$.

mixed flames with some limitations in interpretation, although recently spatially resolved instruments that can also estimate local ϕ have been developed [21].

The dynamics of the flame to imposed inlet velocity oscillations was captured using OH*, FSD, and RX imaging techniques. All these measurements, when using data only from the vortex-dominated region, showed a definite increase in phase-averaged heat release rate when the vortex appeared. However, the global heat release measurements (i.e., including data from the whole domain) showed a decrease in heat release at the same phase relative to the forcing. The phase-averaged FSD and OH* imaging also showed a decreased heat release in regions above the vortex when the vortex was close to the bluff body. The measurements hence suggest the possibility of flame surface destruction or flame annihilation away from the bluff body, downstream from the vortex. Thus, the balance between the fluctuations in local heat release by vortex rollup and by cusp formation and flame annihilation resulted in the global heat release modulation.

This conjecture was tested with examination of time series of OH PLIF. Fig. 20 is a typical time sequence of the OH PLIF images. It shows the flame surface evolution with time when subjected to strong inlet velocity perturbations. It was observed from these measurements that the vortex induced by velocity fluctuations was convected with a velocity approximately equal to the bulk velocity at the dump plane and the vortex grew in size. The important observation during this measurement is that the vortex brought together the flame elements stabilised on the

inner and outer shear layer (at the interface of inner and outer recirculation zone, respectively) and this interaction resulted in flame surface destruction (marked with circle labelled A in Fig. 20). Similar flame annihilation events were observed when different flame elements interacted close to the vortex (marked by square labelled as B in Fig. 20).

These measurements along with the phase-averaged FSD measurements suggest that the flame surface modulation plays a major role in heat release magnitude. It seems that the flame burning rate fluctuations along the flame surface, despite being present (e.g., account for the difference in FSD and OH* data in Figs. 8 and 11 and the difference in FSD and RX data in Fig. 10), are of smaller importance than the magnitude of the flame surface density and how this is altered by the vortices. The latter effect depends conceivably on the laminar burning velocity and hence the difference in the point of saturation in Fig. 16. The former interaction is mostly due to the strain and flame curvature affecting the local burning rate. Laminar strained premixed flames of ethylene have Le > 1 and hence a burning rate reduction is expected [53]. It would be interesting to examine mixtures with Le $= 1$, where strain and curvature effects would be less important.

In an effort to explore this point, measurements with a methane flame at $\phi = 0.7$ that give Le ~ 1 [54] were also taken. This equivalence ratio was selected so that the laminar burning velocity of the flame was the same (~ 0.18 m/s) as the ethylene flame studied here ($\phi = 0.55$). Fig. 21 shows that the methane flame also saturates at approximately the same A value. The
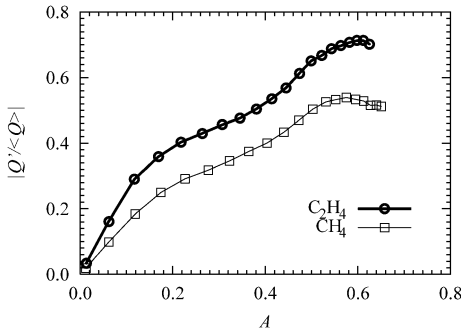
Fig. 21. Comparison of response of ethylene and methane flames of equivalence ratio values $\phi = 0.55$ and 0.7, respectively. Measurements with OH^*, and for both $\langle U \rangle = 9.9$ m/s, $f = 160$ Hz.

$Q'/\langle Q \rangle$ value from OH^* in ethylene is higher than that of OH^* in methane. The difference of the two curves in Fig. 21 is of similar magnitude to the difference between the OH^* and FSD in ethylene flames (Fig. 11) and both differences should be due to local strain and curvature effects. We may conjecture hence that the flame area modulation is the most important phenomenon affecting the global heat release fluctuations, with localised variations being less important.

4. Conclusions

Detailed experimental investigations were performed to measure the response of lean premixed turbulent bluff-body-stabilised flames to imposed inlet velocity perturbations through transfer function measurements. Special attention was given to the amplitude dependence of the transfer function, since the flame response to high amplitudes is relevant to the emergence of limit-cycle combustion-induced oscillations. Three different heat release measurement approaches were followed during the present work, namely OH^* and CH^* chemiluminescence using photo-multiplier tubes and ICCD, flame surface density (FSD) based on OH PLIF, and local heat release (RX) rate evaluated from simultaneous OH and CH_2O PLIF measurements. The imaging system comprised four Nd:YAG lasers, two dye lasers, and two double-exposure cameras. It was also used to provide a sequence of four OH PLIF images separated by 1 ms, which assisted in showing the time evolution of the flame front during the forcing cycle.

Concerning a comparison of the above techniques used to evaluate the flame transfer function, the following conclusions were reached. First, the global heat release evaluated from OH^* and CH^* chemiluminescence agreed very well both in magnitude and in phase. Second, the magnitude of the heat release

response captured by chemiluminescence measurements and by FSD showed a similar trend with forcing amplitude. Finally, the local heat release evaluated from high-resolution reaction rate imaging was higher than that estimated from the FSD measurement by 10–20% in magnitude and the latter had a phase lag of about 40°. These results show that the heat release estimation through measurement of the flame surface density is adequate for flame instability studies, despite the large amplitudes of forcing used here. This implies that the local effects of strain and curvature in reducing the burning velocity probably do not cause large variations in the global heat release rate.

Concerning the detailed flame response with forcing amplitude, it was found that the heat release increased nonlinearly after inlet velocity amplitudes of around 15%, a value that depended on the forcing frequency and the equivalence ratio. This nonlinearity was found to occur when the reacting shear layers rolled up into vortices and was captured with all heat release measurement techniques. The vortices induced by the inlet velocity fluctuations not only generated flame area when the flame wrapped around them but also caused cusps and even large-scale flame annihilation events, as observed in time-resolved OH PLIF images, when parts of the flame stabilised on the inner shear layer close to the recirculation zone collapsed on parts of the flame stabilised on the outer recirculation zone, a phenomenon that was made more prominent with increasing forcing amplitude. A further nonlinearity occurred at high amplitudes and at some equivalent ratios, where a significant leakage of energy to higher harmonics was observed, despite the fact that the inlet velocity fluctuation had a correspondingly small content at the harmonic frequency.

The present results suggest that the flame sheet kinematics play a major role in the saturation mechanism of lean premixed flame response, hence extending previous experimental and analytical results from laminar to turbulent flames. Heat release fluctuations due to local fluctuations of strain rate and curvature had a smaller effect, while no localised extinction has been observed even at large forcing amplitudes.

References

[1] A.P. Dowling, S.R. Stow, J. Propul. Power 19 (2003) 751–764.

[2] S. Candel, Proc. Combust. Inst. 29 (2002) 1–28.

[3] A.P. Dowling, J. Fluid Mech. 346 (1997) 271–290.

[4] F. Baillot, D. Durox, R. Prud'Homme, Combust. Flame 88 (1992) 149–168.

[5] S. Ducruix, D. Durox, S. Candel, Proc. Combust. Inst. 28 (2000) 765–773.

[6] T. Schuller, D. Durox, S. Candel, Combust. Flame 134 (2003) 21–34.

[7] T. Lieuwen, J. Propul. Power 19 (2003) 765–781.

[8] C.J. Lawn, W. Polifke, Combust. Sci. Technol. 176 (2004) 1359–1390.

[9] M. Zhu, A.P. Dowling, K.N.C. Bray, in: Proc. ASME Turb. Expo., 2001, 2001-GT-0374.

[10] S.J. Brookes, R.S. Cant, I.D.J. Dupere, A.P. Dowling, J. Eng. Gas Turb. Power Trans. ASME 123 (2001) 322–326.

[11] P.J. Langhorne, J. Fluid Mech. 193 (1988) 417–443.

[12] C.J. Bloxsidge, A.P. Dowling, P.J. Langhorne, J. Fluid Mech. 193 (1988) 445–473.

[13] C.J. Lawn, S. Evesque, W. Polifke, Combust. Sci. Technol. 176 (2004) 1331–1358.

[14] C. Kulsheimer, H. Buchner, Combust. Flame 131 (2002) 70–84.

[15] K. Zähringer, D. Durox, F. Lacas, Int. J. Heat Mass Transfer 46 (2003) 3539–3548.

[16] T. Lieuwen, Y. Neumeier, Proc. Combust. Inst. 29 (2002) 99–105.

[17] C.J. Lawn, Combust. Flame 123 (2000) 227–240.

[18] W. Pun, S.L. Palm, F.E.C. Culick, Combust. Sci. Technol. 175 (3) (2003) 499–521.

[19] D. Bernier, S. Ducruix, F. Lacas, S. Candel, N. Robart, T. Poinsot, Combust. Sci. Technol. 175 (2003) 993–1013.

[20] Y. Hardalupas, A. Selbach, Prog. Energy Combust. Sci. 28 (2002) 75–104.

[21] Y. Hardalupas, M. Orain, Combust. Flame 139 (2004) 188–207.

[22] Q.V. Nguyen, P.H. Paul, Proc. Combust. Inst. 26 (1996) 357–364.

[23] J.G. Lee, D.A. Santavicca, J. Propul. Power 19 (2003) 735–750.

[24] A.P. Dowling, J. Fluid Mech. 394 (1999) 51–72.

[25] R. Knikker, D. Veynante, C. Meneveau, Proc. Combust. Inst. 29 (2002) 2105–2111.

[26] C.F. Kaminski, J. Hult, M. Alden, S. Lindenmaier, A. Dreizler, U. Mass, M. Baum, Proc. Combust. Inst. 28 (2000) 399–405.

[27] M.Z. Haq, C.G.W. Sheppard, R. Woolley, D.A. Greenhalgh, R.D. Lockett, Combust. Flame 131 (2002) 1–15.

[28] T.C. Chew, K.N.C. Bray, R.E. Britter, Combust. Flame 80 (1990) 65–82.

[29] I.G. Shepherd, Proc. Combust. Inst. 26 (1996) 373–379.

[30] D. Veynante, J.M. Duclos, J. Piana, Proc. Combust. Inst. 25 (1994) 1249–1256.

[31] B.M. Descamps, G.J. Smallwood, J. Prieur, D.R. Snelling, O.L. Gulder, Proc. Combust. Inst. 26 (1996) 427–435.

[32] S.-Y. Lee, S. Seo, J.C. Broda, S. Pal, R.J. Santoro, Proc. Combust. Inst. 28 (2000) 775–782.

[33] H.N. Najm, P.H. Paul, C.J. Mueller, P.S. Wyckoff, Combust. Flame 113 (1998) 312–332.

[34] P.H. Paul, H.N. Najm, Proc. Combust. Inst. 27 (1998) 43–50.

[35] S. Böckle, J. Kazenwadel, T. Kunzelmann, D.I. Shin, C. Schultz, J. Wolfrum, Proc. Combust. Inst. 28 (2000) 279–286.

[36] A. Fayoux, K. Zähringer, O. Gicquel, J.C. Rolon, Proc. Combust. Inst. 30 (2005) 251–257.

[37] H.N. Najm, O.M. Knio, P.H. Paul, P.S. Wyckoff, Combust. Sci. Technol. 140 (1998) 369–403.

[38] B.D. Bellows, Q. Zhang, Y. Neumeier, T. Lieuwen, B.T. Zinn, in: 41st AIAA Aerospace Sci. Meet. Exhibit, Reno, NV, 2003, AIAA-2003-824.

[39] Y. Huang, V. Yang, Combust. Flame 136 (2004) 383–389.

[40] T.J. Poinsot, A.C. Trouve, D.P. Veynante, S. Candel, E.J. Esposito, J. Fluid Mech. 177 (1987) 265–292.

[41] K.C. Schadow, E. Gutmark, Prog. Energy Combust. Sci. 18 (1992) 117–132.

[42] A. Bourehla, F. Baillot, Combust. Flame 114 (1998) 303–318.

[43] T. Schuller, D. Durox, S. Candel, Combust. Flame 135 (2003) 525–537.

[44] Preetham, T. Lieuwen, in: 40th AIAA/ASME/SAE/ASEE Joint Propul. Conf. Exhibit, Fort Lauderdale, FL, 2004, AIAA-2004-4035.

[45] A.F. Seybert, D.F. Ross, J. Acoust. Soc. Am. 61 (1977) 1362–1370.

[46] B.O. Ayoola, R. Balachandran, J.H. Frank, E. Mastorakos, C.F. Kaminski, submitted for publication.

[47] N.T. Clemens, in: J.P. Hornak (Ed.), Encyclopedia of Imaging Science and Technology, Wiley, New York, 2002, p. 390.

[48] J.M. Donbar, J.F. Driscoll, C.D. Carter, Combust. Flame 122 (2000) 1–19.

[49] R. Giezendanner, O. Keck, P. Weignand, W. Meier, U. Meier, W. Stricker, M. Aigner, Combust. Sci. Technol. 175 (2003) 721–741.

[50] C.E.C. Cala, E.C. Fernandes, M.V. Heitor, in: 11th Symposium on Application of Laser Techniques and Fluid Mechanics, Lisboa, Portugal, 2002.

[51] B.D. Bellows, T. Lieuwen, in: 42nd AIAA Aerospace Sci. Meet. Exhibit, Reno, NV, 2004, AIAA-2004-0455.

[52] C.A. Armitage, A.J. Riley, R.S. Cant, A.P. Dowling, S.R. Stow, in: Proc. ASME Turb. Expo., 2004, 2004-FT-53820.

[53] C.J. Rutland, A. Trouve, Combust. Flame 94 (1993) 41–57.

[54] M. Mizomoto, H. Yoshida, Combust. Flame 70 (1987) 47–60.